On the S/Z Relationship for Rimed Snow Particles in the W-band

Shelby Fuller [1], Sam Marlow [1], Samuel Haimov [1], Matthew Burkhart [1], Kevin Shaffer [1], Austin Morgan [1], and Jefferson R. Snider [1,2]

[1] Department of Atmospheric Science, University of Wyoming, Laramie, WY, USA

[2] Corresponding Author, jsnider@uwyo.edu

Abstract

Values of liquid-equivalent snowfall rate (S) at a ground site and microwave reflectivity (Z) retrieved using an airborne W-band radar were acquired during overflights. The temperature at the ground site was between -6 and -15 ^{o}C. At flight level, within clouds containing ice and supercooled liquid water, the temperature was approximately 7 ^{o}C colder. Additionally, airborne measurements of snow particle imagery were acquired. The images demonstrate that most of the snow particles were rimed. A relatively small set of S/Z pairs (4) are available from the overflights. Important distinctions between these measurements and those of Pokharel and Vali (2011), who also reported S/Z pairs for rimed snow particles, are 1) the fewer number of data pairs, 2) the method used to acquire S, and 3) the altitude of the Z retrievals. It also shown that a computationally-based S/Z relationship applied in W-band retrievals can underestimate S by approximately a factor of two when snowfall is produced by riming.

1 - Introduction

Improvement of methods used to measure snowfall and rainfall are an ongoing focus of meteorological research. The various methods are ground-based instruments that evaluate the mass of precipitation that falls into or onto a collector (precipitation gauges) (Brock and Richardson 2001), ground-based radars (Wilson and Brandes 1979), and airborne and space-borne radars (Matrosov 2007; Kulie and Bennartz 2009; Geerts et al. 2010; Skofronick-Jackson et al. 2017). An objective of these approaches, whether used to make observations independent of other methods (e.g., Kulie and Bennartz 2009), or as a component of multiple observations (e.g., Cocks et al. 2016), is estimation of precipitation rate and accumulation.

Many studies have investigated using radar for evaluating rainfall (for a review see Wilson and Brandes 1979). There are two approaches. The first is research, both observational and computational, that probes the relationship between rainfall rate (R) and radar-measured values of backscattered microwave power. The latter is commonly reported as an equivalent radar reflectivity factor (Z_e). The second is operational in the sense that precipitation gauges are used to calibrate measurements acquired using weather surveillance radars. Complications associated with converting Z_e to R, or converting a radar reflectivity factor[1] (Z) to R, can be grouped in four categories: 1) Inaccuracy in quantification of Z, 2) variation of the R/Z relationship stemming from precipitation processes (e.g., coalescence and break up), 3) difference between the volume of a radar range gate versus the much smaller volume of atmosphere sampled as precipitation falls to a gauge, and 4) vertical displacement between a radar range gate and a calibrating gauge, especially at far ranges.

[1] Radars are calibrated to report Z_e (Smith 1984). Herein, radar reflectivities are reported as $Z = Z_e$ and as $dBZ = 10\log_{10}(Z_e)$.

For situations with snowfall, methods employing either gauge or radar are associated with complications beyond that incurred in rainfall (Matrosov 2007; Martinaitis et al. 2015; Cocks et al. 2016). Problems associated with gauge measurements are wind-induced snow particle undercatch, gauge capping, delayed registration, and blowing snow aliasing as snowfall. Moreover, in a situation with snow particles most abundant within a radar range gate, compared to rain drops, and where a measurement of Z is used to infer R via a R/Z relationship, the resultant precipitation rate will likely be inaccurate. This is because hydrometeor shape, density, and dielectric properties are all variable for snow particles while relatively invariant for rain drops. Additionally, a snow particle's terminal fall speed varies with size (as is the case for drops) and with particle shape and particle density. Going forward, we refer to the latter two properties as shape and density.

The goals of this paper are as follows: 1) to describe measurements of undercatch-corrected liquid-equivalent snowfall rate (S, mm h^{-1}) and how these were paired with W-band measurements of reflectivity (Z, mm^6 m^{-3}) ; 2) to contrast the measurement-based S/Z pairs against calculated S/Z relationships commonly applied in retrievals of S based on reflectivity; and 3) to investigate why the acquired data set deviates from predictions of some calculated S/Z relationships.

In calculations of paired values of S and Z, density is an important parameter. Density is commonly estimated using empirical data (e.g., Pokharel and Vali 2011, [PV11]). For graupel, a snow particle that grows via collection of supercooled cloud droplets in a process commonly referred to as riming, paired observations of particle mass and particle size have been used to estimate density. There is considerable uncertainty in this approach. Based on data collected at two northwestern US surface sites (Zikmunda and Vali 1972; Locatelli and Hobbs 1974), density values differ by at least a factor of two at particle sizes smaller than 2000 μm (PV11; their Figure 4). Given that the density of rime ice varies with droplet impact speed, droplet size, and temperature (Macklin 1962), it is not surprising that the density-versus-size relationships analyzed by PV11 are so varied.

The following introductory paragraphs overview W-band S/Z relationships being applied in instances of snowfall where mass is acquired by vapor deposition (crystal), by collection of crystals (aggregate), and by riming (rimed crystals and graupel). Henceforth, the latter two snow particle types are collectively referred to as rimed snow particles.

In a computational study, Hiley et al. (2011) considered a variety of snow particle types (column, plate, bullet rosette, sector plate, dendrite, and aggregate), employed a parameterized ice particle size distribution (PSD) function (Field et al. 2005), accounted for a range of temperature (-5 to -15 ^{o}C) via the Field et al. parameterization, and developed a range of S/Z relationships for snow particles. Except for the aggregates, the modeled particle types were crystals. Hiley et al.'s upper- and lower-limit relationships are $S = 0.21 \cdot Z^{0.77}$ and $S = 0.024 \cdot Z^{0.91}$. Matrosov (2007) developed a range of S/Z relationships for aggregates. In that work, PSDs from Braham (1990) were employed, and a range of particle aspect ratios and densities were factored into the calculations. For aggregates, the S/Z relationship is $S = 0.056 \cdot Z^{1.25}$ and the upper- and lower-limit S/Z relationships are $S = 0.11 \cdot Z^{1.25}$ and $S = 0.041 \cdot Z^{1.25}$ (Matrosov 2007). It should be noted that Hiley et al. (2011) and Matrosov (2007) employed similar, but not identical, computational methods and parameterized mass-size relationships. Kulie and Bennartz (2009) developed an S/Z relationship for what they referred as a "snow particle" type. The wavelength-dependent density derived by Surussavadee and Staelin (2007) (200 kg m^{-3} at λ = 3.2 mm) was adopted, the snow particles were modeled as spheres, and the Field et al. parameterization was applied. The S/Z relationship developed for this particle type is $S = 0.52 \cdot Z^{0.83}$ (Surussavadee and Staelin 2007; Kulie and Bennartz 2009; henceforth SSKB). Variance in the calculations discussed in this paragraph originate from changes in density, shape, fall speed, and PSD as these changes are propagated through the cloud-microphysical and microwave-scattering calculations.

In a hybrid approach (computational and an analysis of airborne observations), PV11 concluded that most of the snow particles they imaged were rimed snow particles. Their calculations of S and *Z*, conducted using two density-size relationships (indicated with ρ_1 and ρ_3), were presented. They compared their calculated reflectivities to measurements of Z from a W-band radar. That led to their conclusion that "...the lower density assumption…yielded closer correspondence to observed reflectivities." Their recommendation for S as a function of Z - hereafter the $S(\rho_1)/Z$ best-fit line - is $S = 0.39 \cdot Z^{0.58}$. In addition to variance in their values of S, coming from a dependence on density, PV11 state that a value of S derived via their best-fit line is uncertain by a factor-of-ten. That uncertainty is evident in the variance seen about the line in Fig. 11 of PV11. Those investigators, and Geerts et al. (2010), attributed the variance to use of two-dimensional snow particle imagery in calculations of S and to actual variations of density and shape not accounted for in the calculations.

Our focus is on surface measurements of S and on pairing of those measurements with airborne measurements of Z. We also analyze airborne measurements of snow particle imagery. The latter demonstrates that the particles observed at flight level were rimed. These measurements are the basis for our assertion that our data set is relevant to ongoing investigations of using Z to evaluate S in situations where precipitation is produced by riming.

Section 2 describes the setting of our study, the instruments we deployed, and recordings we obtained using two data acquisition systems. One of the data systems was operated at a ground site and the other on an aircraft. Section 3 is an analysis of the recordings; this section also considers recordings from two additional, but ancillary, ground sites. Our findings are discussed in Sect. 4 and summarized in Sect. 5. An Appendix (Sect. 6) explains how we averaged recordings of near-surface W-band reflectivities and surface-based recordings of snowfall.

2 - Site, Aircraft, and Instruments

2.1 - Site

We analyzed aircraft and ground data from 14/15 December 2016, when the analyzed snowfall event spanned a UTC date change, and from 3 January 2017. The ground data were acquired in a forest/prairie ecotone on the eastern slope of the Medicine Bow Mountains in southeastern Wyoming (Figs. 1a-b). No ground-based observers were deployed during the two snowfall events we analyzed.

At one of three ground sites (HP in Figs. 1a-b) we deployed a hotplate precipitation gauge (Rasmussen et al. 2011; Zelasko et al. 2018), a GPS receiver, and a data acquisition system. Once per second, the data system ingested a hotplate-generated data string, combined that with time-of-day from the GPS receiver (Coordinated Universal Time (UTC)), and recorded the merged hotplate/UTC data string. The absolute accuracy of the time stamp is no worse than 2 s.

Overflights of the hotplate were done by the University of Wyoming King Air (WKA) on 14/15 December 2016 and on 3 January 2017. Data acquisition on the WKA was also synchronized with UTC, but with much better accuracy than at the hotplate. Measurements of horizontal wind (speed and direction), temperature, relative humidity, and pressure from the US-GLE AmeriFlux tower (AF in Figs. 1a-b) are also components of our analysis. The AmeriFlux data were provided to us as 30-minute averages (AmeriFlux 2021; Marlow et al. 2023).

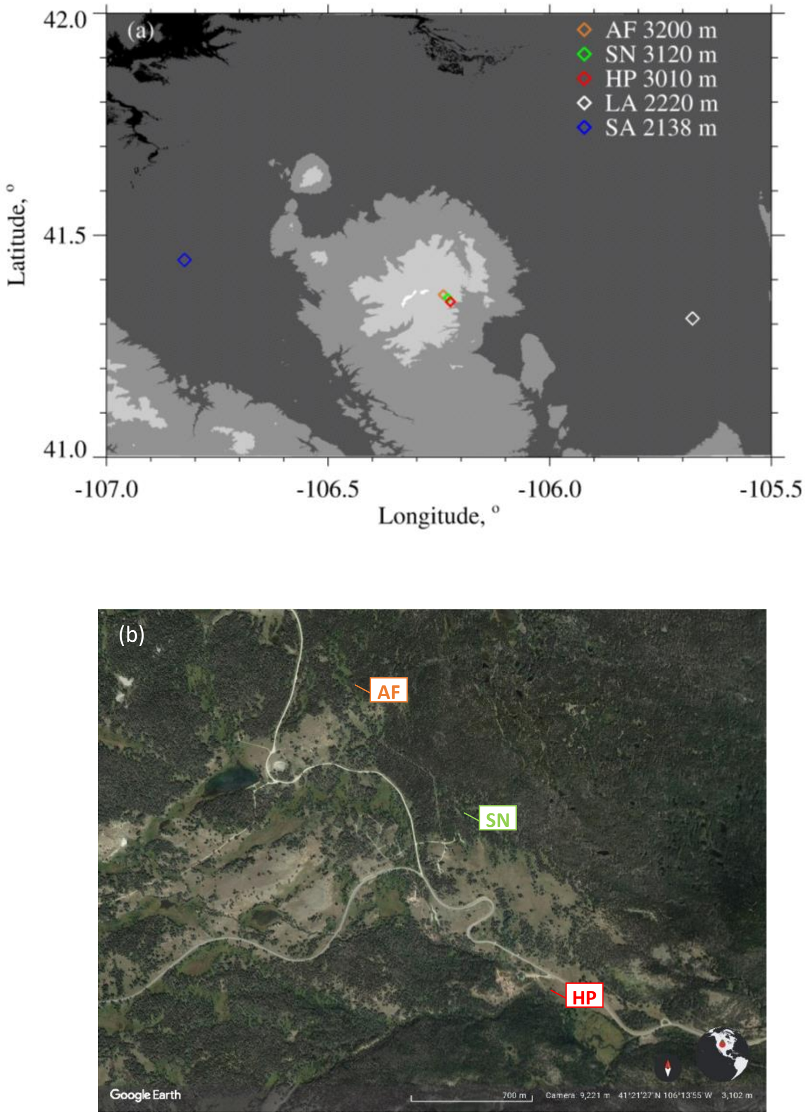

Figure 1 – (a) Southeast Wyoming, airport at Saratoga, WY (SA), airport at Laramie, WY (LA), and the ground sites: AF = US-GLE AmeriFlux tower, SN = Brooklyn Lake SNOTEL, and HP = hotplate. Altitudes of the airports and ground sites are in the legend. Altitude thresholds for the digital elevation map are 1500, 2000, 2500, 3000, and 3500 meters. (b) Close up of the AF, SN, and HP ground sites (from © Google Earth).

2.2 - University of Wyoming King Air (WKA)

The following WKA measurements were analyzed: aircraft position, temperature, snow particle imagery, and three moments of the cloud droplet size distribution function. A Cloud Droplet Probe (CDP; Faber et al. 2018) was the basis for the droplet size distribution measurements and the derived moments. The latter are droplet concentration (N), cloud liquid water content (LWC), and mean droplet diameter (<D>). Snow particle imagery was obtained using a precipitation particle imaging probe (2DP; Korolev et al. 2011) and a cloud particle imaging probe (2DS; Lawson et al. 2006). These acquired two-dimensional images of particles between 200 to 6400 μm (2DP) and between 10 to 1280 μm (2DS).

2.3 – The W-band Wyoming Cloud Radar (WCR)

Retrievals from the up-looking and down-looking antennas of the WCR, operated on the WKA, were also analyzed. For this we used Level 2 WCR data[2] with reflectivities recorded as $dBZ = 10 \cdot \log_{10}(Z)$. The reflectivities were converted from dBZ to Z prior to processing. Additionally, values of the vertical-component Doppler velocity retrieved from below the WKA using the WCR's down-looking antenna were analyzed. The Doppler velocities were corrected for aircraft motion, as described in Haimov and Rodi (2013). We use V_D to symbolize the corrected vertical-component Doppler velocity and adopt the convention that $V_D > 0$ indicates upward hydrometeor motion.

[2] http://flights.uwyo.edu/uwka/wcr/projects/snowie17/PROCESSED_DATA/

The Level 2 WCR sampling was different on the two flight days and this difference is indicated in Table 1. The flights were conducted in preparation for the SNOWIE field project (Tessendorf et al. 2019) and were flown from the Laramie, WY Airport ("LA" in Fig. 1a).

Ground-based calibrations of the WCR's up-looking antenna and correlations between in-flight retrievals acquired using the WCR's up-looking and down-looking antennas were used to estimate the absolute accuracy of the WCR-derived values of dBZ. This is ±2.5 dBZ (PV11).

Table 1 – Level 2 WCR sampling and the WKA overflight time

Date	Level 2 WCR Vertical Sampling, m	Level 2 WCR Along-track Sampling, s	Overflight Time, UTC
14/15 December 2016	23	0.23	00:00:38 (15 December 2016)
3 January 2017	30	0.36	20:32:03

2.4 - Hotplate Gauge

Algorithms used to process hotplate measurements are described in Rasmussen et al. (2011), Boudala et al. (2014), and Zelasko et al. (2018). Henceforth, these are referred to as R11, B14, and Z18, respectively. This section describes how hotplate measurements acquired at the HP site were analyzed.

Four measurements fundamental to the steady state energy budget of the hotplate's temperature-controlled up-viewing plate are output by the hotplate microprocessor as one-minute running averages (Z18). These averages were merged with the GPS time and recorded at 1 Hz by the data acquisition system (Sect. 2.1). The four measurements are electrical power supplied to the plate, ambient temperature, wind speed, and solar irradiance. With these measurements, calibration data (Marlow et al. 2023), and the algorithm developed by Z18, we calculated a liquid-equivalent snowfall rate. The latter was not corrected for snow particle undercatch; however, in what follows we describe that correction.

Marlow et al. (2023; their Figure 4b) report the relationship between snow particle catch efficiency and wind speed that we applied in calculations of the undercatch-corrected liquid-equivalent snowfall rate. There are three bases for this relationship. First is the catch efficiencies R11 derived using measurements obtained from a weighing gauge, operated within a double fence intercomparison reference shield, and collocated measurements from an unshielded hotplate gauge. We symbolize these paired measurements as SRG (shielded reference gauge) and UHG (unshielded hotplate gauge). R11 plotted hotplate catch efficiencies (i.e., UHG/SRG) versus wind speeds measured at 10 m AGL (their Fig. 8). Second is Marlow et al.'s adjustment of R11's 10 m AGL wind speeds to 2 m AGL. The basis for the adjustment is surface boundary layer parameters derived for R11's site (Kochendorfer et al. 2018) and an equation from

Panofsky and Dutton (1984; their Eq. 6.7). The adjustment was made because the hotplate-derived wind speeds, both here and in Marlow et al. (2023), were acquired at approximately 2 m above the snowpack surface. Third is Marlow et al.'s comparison of SNOTEL-derived snow water equivalent depth changes and hotplate-derived time-integrated accumulations. The time-base for the comparisons was 24 hours. Based on that comparison, which has 57 paired values acquired at the sites labeled HP and SN in Fig. 1, the average fractional absolute relative difference is 0.30. In the Marlow et al. (2023) comparison (their Fig. 9a), at accumulation = 10 mm, imprecision associated with the SNOTEL measurement corresponds to a relative error which is 0.24 (Marlow et al. 2023). This indicates that SNOTEL contributed significantly to the previously-mentioned relative difference and especially so for the smaller accumulations in Figure 9a of Marlow et al. (2023). Because of this, we did not limit calculation of the relative difference to a subset of the 57 paired measurements. Based on this assessment of the relative difference, the hotplate precision applied in this analysis was taken to be 0.3.

The hotplate-derived wind speeds acquired at ~ 2 m, and discussed in the previous paragraph, are henceforth symbolized U_{PRO}. The basis for these is a steady state energy budget of the hotplate's temperature-controlled down-viewing plate and a proprietary algorithm (R11 and Z18). The U_{PRO} are reported by a hotplate as one-minute running averages (Z18) and we recorded these at 1 Hz. Examples are the gray dots in Fig. 2. Additionally, we calculated and analyzed one-minute-averaged values of U_{PRO} and the corresponding standard deviations. Examples of these are the black circles and the short vertical line segments in Fig. 2.

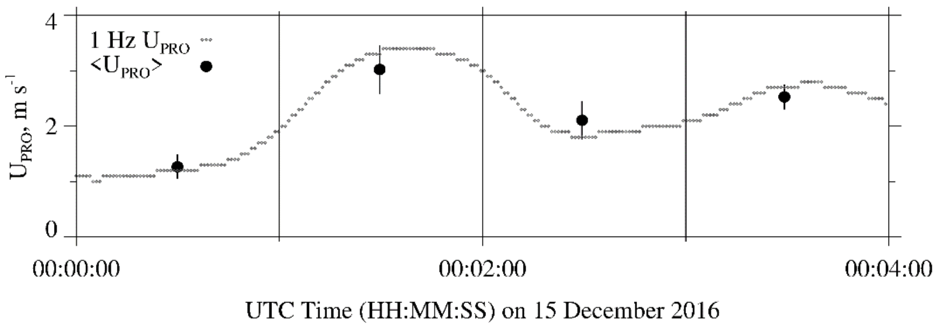

Figure 2 – Hotplate wind speed measurements (U_{PRO}) 00:00:00 to 00:04:00 on 15 December 2016. Gray dots are the one-minute running-average U_{PRO} recorded at 1 Hz. Black circles are the one-minute-averaged U_{PRO} (± 1 standard deviation).

3 - Analysis

3.1 - WKA Overflight Time

The focus of our analysis is the two WKA flight segments shown in Figs. 3a-b. The maps shown in the figures have the three ground sites (AF, SN, and HP) and the WKA flight tracks (white line). The beginning-to-end time interval for the flight tracks is 100 s and these are divided into ten 10-second intervals. The 10 s intervals are indicated with white diamonds. Except for the turn evident in Fig. 3b, the flight tracks are straight, and the track direction is approximately upwind to downwind.

Times that the WKA was closest to the HP site were evaluated by finding the point on the flight track where the horizontal position of the WKA was closest to the hotplate's coordinates. These times are symbolized t_O and are referred to as overflight times. In Figs. 3a-b the downwind end of the flight tracks end at the overflight time. The latitude/longitude position of the aircraft was within 390 m of the hotplate at the overflight times. Table 1 has the overflight times on the two flight days.

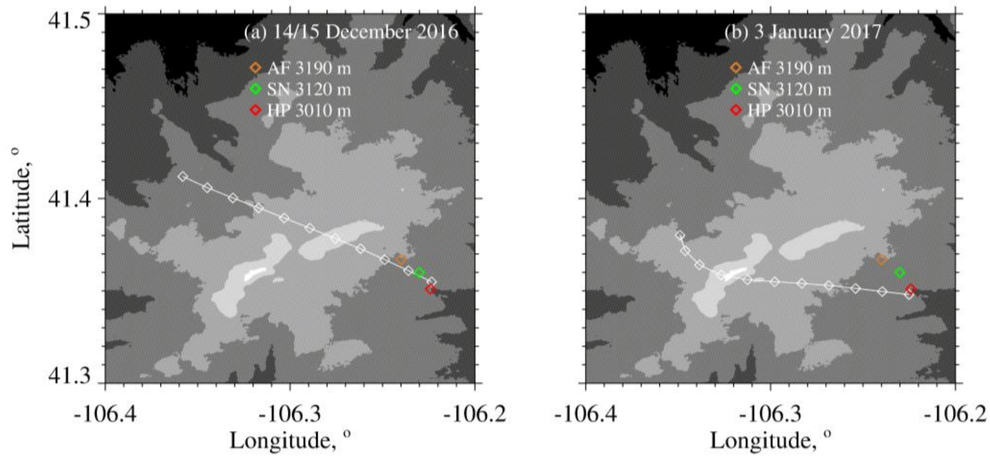

Figure 3 – (a) WKA flight track on 14/15 December 2016 for time interval = overflight time - 100 s to the overflight time. (b) WKA flight track on 3 January 2017 for time interval = overflight time - 100 s to the overflight time. The white diamonds on the tracks are separated, in time, by 10 s. Altitude thresholds for the digital elevation maps are 2600, 2800, 3000, 3200, 3400, and 3600 meters. Altitudes of the ground sites are in the legend.

3.2 – Effect of Attenuation on WCR Reflectivities

(NOTE: Table 3 is at the end of the manuscript)

The presence of water vapor, cloud water, and snow particles within the WCR's transmission path will contribute to an attenuation of microwave intensity and will therefore negatively bias the retrieved reflectivities (Matrosov 2007; Hiley et al. 2011; Kneifel et al. 2015). We used *in situ* measurements, and models of attenuation, to estimate this bias. For vapor, we used temperature (T), relative humidity (RH), and pressure (P) measurements from the AF (Table 2) and an equation for the extinction coefficient (Ulaby et al. 1981; their Eq. 5.22). For cloud water, we used T and LWC measurements from the WKA and a parameterized extinction coefficient (Liebe et al. 1989; Vali and Haimov 2001). For snow particles, we used 2DP-derived snow particle mass concentrations, from the WKA, and extinction measurements from Nemarich et. al (1988). The snow mass concentrations were evaluated as the product of the 2DP-derived snow particle volume - assuming spheres - and a snow particle density ρ = 210 kg m^{-3}. This estimate of density comes from PV11's ρ_1 formula evaluated at D = 1 mm. Vapor, cloud water, and ice particle concentrations applied in the calculations are in the second to fourth columns of Table 3. These are the maxima of measurements acquired between t_o - 10 s and t_o. This time interval is nearly the same as the combined durations of the two WCR averaging intervals analyzed in Sect. 3.5. The fifth to seventh columns have the one-way transmission pathlengths. For cloud water, this is the vertical distance between cloud base [derived thermodynamically using AF measurements (Table 2)] and the flight level, and for both vapor and snow particles this is the vertical distance between the hotplate and the flight level. (Aircraft and HP altitudes are in Table 2 and Fig. 3.) It was assumed that the measured mass concentrations (vapor, cloud water, and snow particles) were uniform over the prescribed pathlengths. Finally, our use of vapor density from the AF ground site is estimated to have caused the vapor-induced attenuations to be overestimated by approximately 50 %. Two-way attenuations ($\Delta(dB)$), summed over contributions from the three components, are presented in the final column. Fortuitously, these are equal on the two days but with vapor and snow particles dominating on December 15 and with liquid water dominating on January 3. Attenuation-corrected reflectivities (Z') were derived using the uncorrected reflectivities (Z) and the $\Delta(dB)$

$$Z' = 10^{\left[\left(10\cdot\log_{10}(Z)+\Delta(dB)\right)/10\right]}. \tag{1}$$

Table 2 – Atmospheric state averages

Date	WKA [a] Track Altitude, m	WKA [a] T, °C	AF [b] T, °C	AF [b] RH, %	WKA [a, c] Track Vector	WKA [a, c] Wind Vector	AF [b, c] Wind Vector
14/15 December 2016	4546	-13.9	-6.3	86	310 / 130	274 / 32	250 / 8.5
3 January 2017	4196	-21.7	-14.6	77	280 / 120	265 / 27	260 / 5.4

[a] Altitude, temperature, track vector, and horizontal wind vector data obtained by averaging 1 Hz WKA measurements. The averaging interval is 60 s and the interval starts at the overflight time, minus 60 s, and ends at the overflight time.

[b] Temperature (T), relative humidity (RH), and horizontal wind vector data from sensors on the US-GLE AmeriFlux tower (Sect. 2.1). The wind sensor was deployed at 26 m AGL (3223 m MSL) and the T/RH sensor was deployed at 23 m AGL (3220 m MSL). The AF measurements correspond to 30-minute averages closest to the overpass time. In the AF data set time stamps on the relevant AF recordings are 00:00 UTC (15 December 2016) and 20:30 UTC (3 January 2017).

[c] Vectors are presented in the following format: Direction of motion (degree relative to true north) / speed (m s^{-1}).

3.3 - Correction of Doppler Velocity

We accounted for bias in V_D (Sect. 2.3) due to deviation of the down-looking WCR antenna from vertical. This was done by applying the correction described in Zaremba et al. (2022) (their Eq. A4). The west-to-east and south-to-north particle velocities used in the correction were assumed to be equal to component wind velocities. The latter were expressed as linear functions of altitude using the information in the penultimate and last columns of Table 2. The component velocities as functions of altitude and the linear equations relating velocity and altitude are provided in the Appendix.

3.4 - Hotplate Measurement of Wind Speed

Here we compare the hotplate-derived wind speed to wind speed derived using an R.M.Young rotating anemometer (R.M.Young 2001). The second of these symbolizes U_{RMY} and the basis for the first (U_{PRO}) is a proprietary algorithm (Sect. 2.4). We are doing this comparison because B14 showed that U_{PRO} can be high-biased, relative to a conventional anemometer, and because U_{PRO} is the primary determinant of the rate that the up-viewing plate dissipates sensible heat energy. Diagnosis of that heat transfer rate is our basis for calculating the liquid-equivalent snowfall rate (Z18). The U_{PRO} also determines the snow particle catch efficiency and the latter was used in calculations of the undercatch-corrected liquid-equivalent snowfall rate (Sect. 2.4).

Three years before the wind speed comparison presented here, we attempted to compare the U_{PRO} reported by our hotplate[3] and wind speed reported by a WXT520 Vaisala weather transmitter equipped with an ultrasonic anemometer (Vaisala 2012). These instruments were operated at the HP site in Fig. 1b. However, that data set was difficult to interpret because we did

[3] The hotplate used here is the device described in Wolfe and Snider (2012), in Z18, and in Marlow et al. (2023).

not correctly record the desired 1 Hz wind speed measurements from the WXT520. The comparison reported here was done at the Laramie, WY Airport in December 2019 and January 2020. Compared to the HP site, the Laramie Airport site (indicated LA in Fig. 1) is free of obstruction, out to 120 m, and experiences larger wind speeds. By mounting the hotplate and the R.M.Young anemometer on rigid metal pipes, the hotplate's heated horizontal surfaces (the up- and down-viewing plates seen in Figure 1 of Z18) and the anemometer's spinning axis (oriented horizontally) were both positioned at 2 m AGL. The pipes were separated horizontally by 5 m. There was no precipitation on the days selected for the wind speed comparisons. The values of U_{PRO} and U_{RMY} we analyzed were recorded with a data system that time stamped the 1 Hz U_{PRO} and 1 Hz U_{RMY} with a relative timing accuracy no worse than 1 s.

A wind speed comparison - from 13 December 2019 - is shown in Fig. 4a. U_{PRO} was brought into the comparison by sampling it once per minute from files containing 1 Hz recordings of the one-minute running-average U_{PRO} (Sect. 2.4). U_{RMY} was brought into the comparison by starting with files containing 1 Hz recordings and converting these to one-minute averages. Fig. 4a shows no evidence of bias and Fig. 4b demonstrates that the average absolute departure between the U_{PRO} and U_{RMY} (both one-minute averages) is no larger than 0.5 m s^{-1}. Table 4 has eight more precipitation-free comparisons. Included in the table are temperature and wind speed averaged over the comparison intervals (4 to 20 UTC), the slope of the linear-least-squares fit line (forced through the origin, red line), and the lower and upper quartiles of the slope. The quartiles were calculated using the method of Wolfe and Snider (2012). In contrast to Figs. 4a-b, Figs. 4c-d make the comparison using 1 Hz values of U_{PRO} and U_{RMY}. The larger scatter and larger average absolute departure seen in these panels is a consequence of the hotplate's limited time response, compared to the R.M.Young. We quantify the hotplate's response time in terms of a calculated thermal response time. During wintertime at the Laramie Airport, and with wind speed at 5 m s^{-1}, the down-viewing plate's thermal response time is approximately 60 s (results not shown). Because the temperature of the down-viewing plate is actively controlled, this does not translate to a 60 s lag between changes in wind speed and the hotplate response. The U_{PRO}/U_{RMY} departure is most evident at U_{PRO} > 5 m s^{-1} (Fig. 4d) but this is not a concern for U_{PRO} on 14/15 December 2016 or on 3 January 2017. Snider (2023) demonstrated that the U_{PRO} was less than 5 m s^{-1} at the hotplate during the two WKA overflights.

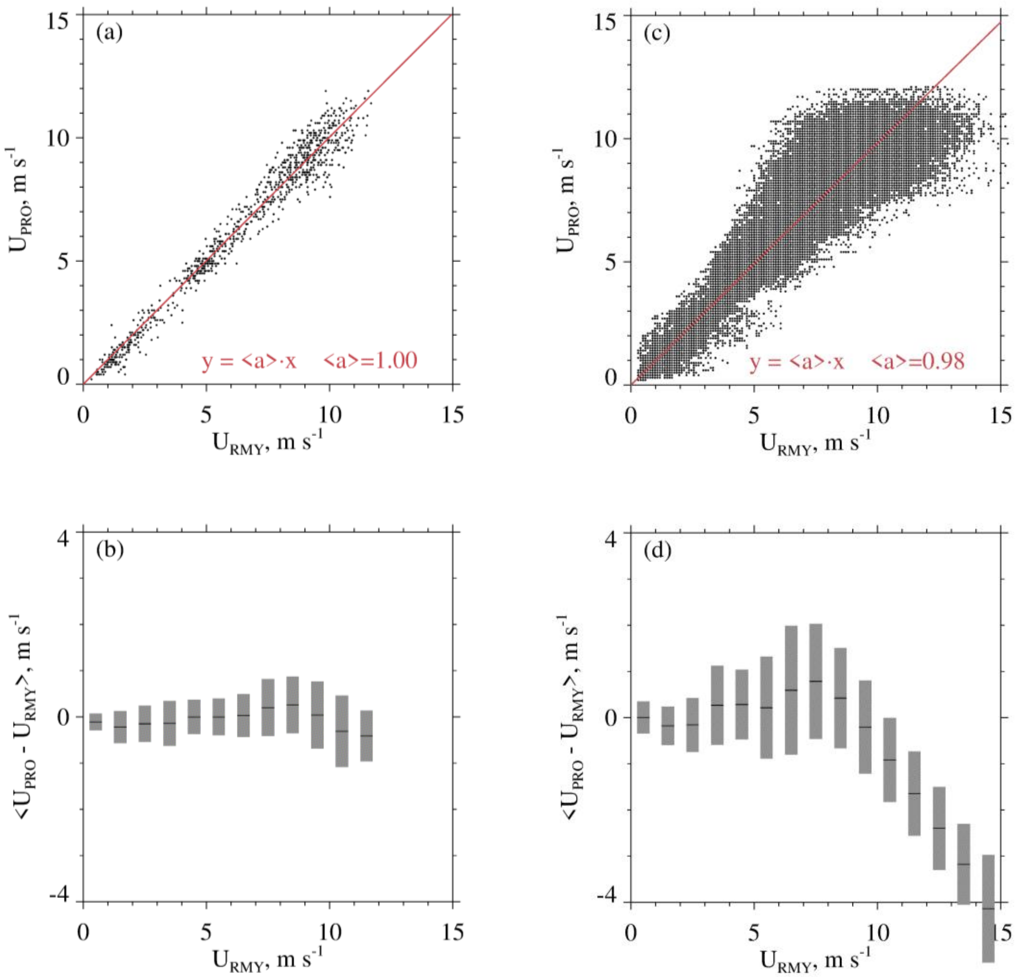

Figure 4 – (a) Scatterplot of one-minute-averaged U_{PRO} and one-minute-averaged U_{RMY}. Measurements were acquired at the Laramie, WY Airport 13 December 2019. The red line is a linear-least-squares fit line (forced through the origin). (b) Average departure between one-minute-averaged U_{PRO} and one-minute-averaged U_{RMY}. Average departures were calculated for discrete U_{RMY} intervals, and the averages are indicated with short black horizontal lines. Gray bars indicate ± 1 standard deviation. (c) Same as in (a) except 1 Hz values of U_{PRO} and U_{RMY}. (d) Same as in (b) except for 1 Hz values of U_{PRO} and U_{RMY}.

Table 4 - U_{PRO} versus U_{RMY} correlations

Date, UTC [1]	<T> [2], °C	<U> [2], m s^{-1}	<a> [3]	a [4] First Quartile	a [4] Third Quartile
7 December 2019	-0.40	5.40	1.00	0.90	1.04
8 December 2019	2.70	4.10	0.99	0.90	1.04
10 December 2019	-5.20	3.80	0.99	0.83	1.04
13 December 2019	-1.50	6.60	1.00	0.93	1.06
18 December 2019	-6.20	3.60	0.99	0.92	1.04
19 December 2019	-6.90	2.70	0.95	0.84	0.99
6 January 2020	-6.40	8.80	1.01	0.96	1.06
8 January 2020	0.30	4.20	1.00	0.87	1.05
11 January 2020	-7.20	7.00	1.02	0.97	1.08

[1] Statistics presented are based on one-minute-averaged U_{PRO} and one-minute-averaged U_{RMY} measurements made between 04:00 to 20:00 UTC.

[2] Interval-averaged temperature and interval-averaged wind speed.

[3] Slope of the one-minute-averaged U_{PRO} versus one-minute-averaged U_{RMY} linear-least-squares fit line, forced through the origin.

[4] Quartiles of the slope (see text)

3.5 – Combined Aircraft and Surface Measurements

Figure 5 has WCR and WKA measurements starting 100 s prior to t_o and ending at t_o. The sequences in Figs. 5a and 5c are reflectivities from both the up- and down-looking antennas. In Fig. 5a the flight track (black dashed horizontal line) is at 4550 m and in Fig. 5c the flight track is at 4200 m. At the t_o in Fig. 5a, below the WKA, the maximum radar echo is +6 dBZ (Z = 4 mm^6 m^{-3}) and in Fig. 5c the maximum is -3 dBZ (Z = 0.5 mm^6 m^{-3}). Supercooled liquid water was detected as the aircraft approached the ridgeline (Fig. 5b) and during the last 10 seconds of the time sequence in Fig. 5d. During these encounters with supercooled liquid, the maximum LWC values were 0.03x10^{-3} and 0.08x10^{-3} kg m^{-3} on 14 December 2016 and 3 January 2017, respectively. Values of N (Sect. 2.2) at times of maximal LWC were 3x10^6 and 100x10^6 m^{-3} on 14 December 2016 and 3 January 2017, respectively. Even on 3 January 2017, the <D> (Sect. 2.2) associated with maximum LWC was sufficient for hexagonal plate crystals with diameter larger than 100 μm to collide with the observed droplets with efficiencies > 0.1 (Wang and Ji 2000).

We temporally and spatially averaged the values of Z we compared with time-averaged values of S. There are two reasons for this: 1) As discussed in Sect. 3.1, the WCR did not sample Z exactly over the hotplate, and furthermore, the width of radar beam at 1500 m range - roughly the distance between the aircraft and the ground at the overflight times - is 30 m and thus considerably smaller than the minimum horizontal distance between the aircraft and the HP. 2) Compared to the WCR, the hotplate is a relatively slow-response measurement system whose output is commonly averaged over one-minute intervals (Z18).

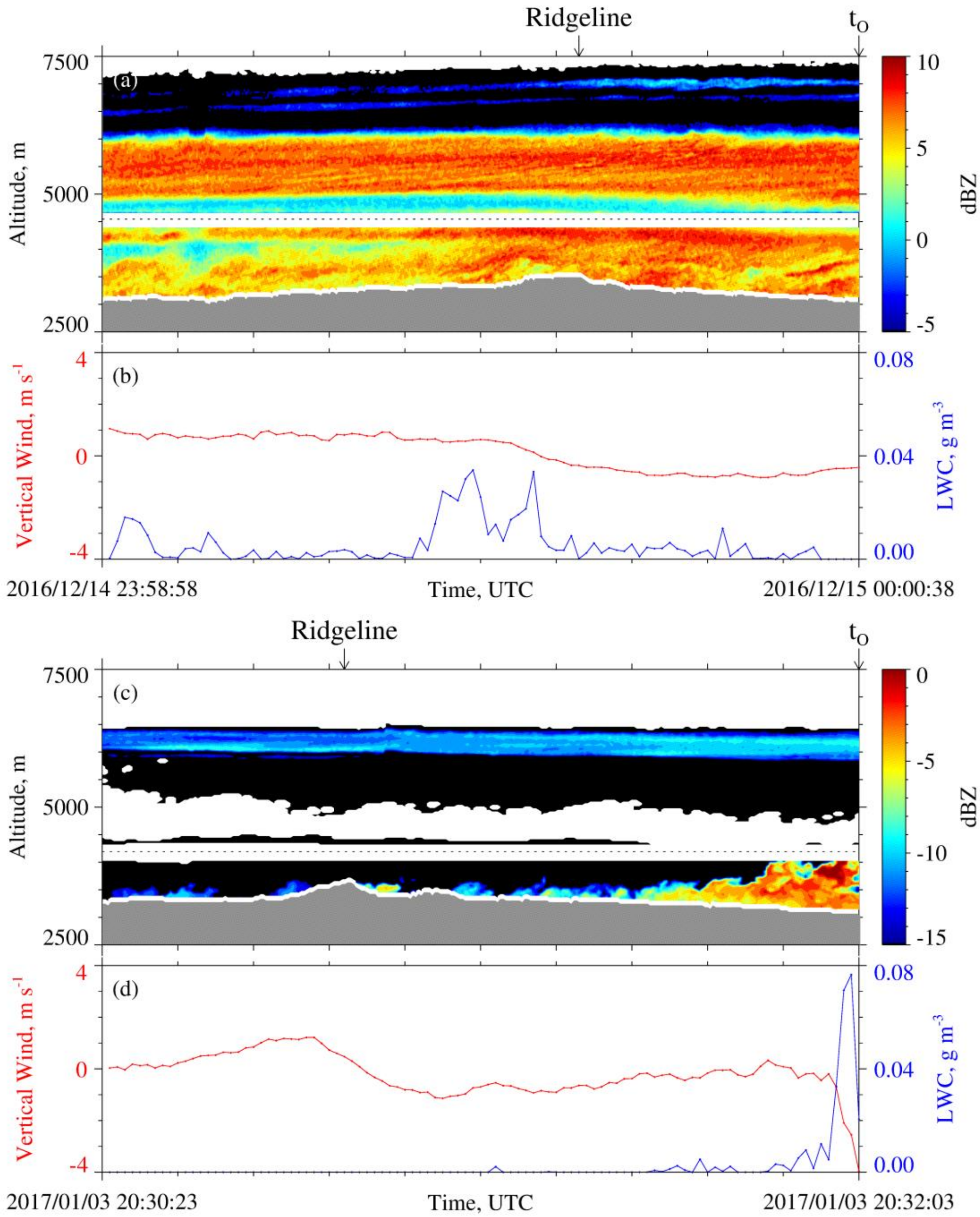

Figure 5 – (a) 100 s of WCR reflectivity and (b) 100 s of LWC and gust probe vertical wind velocity ending at t_o on 14/15 December 2016. (c) 100 s of WCR reflectivity and (d) 100 s of LWC and gust probe vertical wind velocity ending at t_o on 3 January 2017. In (a) and (c) above and below the flight track is the roughly 200-m-deep WCR blind zone, reflectivity above (below) the flight track is from the up-looking (down-looking) WCR antenna, black indicates dBZ values smaller than minimum indicated in the color bar, white immediately above the terrain indicates echo that was discarded because of ground clutter, and white above the ground clutter and outside of the blind zone indicate dBZ < minimum detectable signal.

The HP measurements were averaged over two adjacent 60 s intervals. The first extends from t_O to t_O + 60 s (Fig. 6a) and the second from t_O + 60 s to t_O + 120 s (Fig. 6c). In Fig. 6a and in Fig. 6c, $t_{HP,B}$ symbolizes an interval's beginning time and $t_{HP,E}$ symbolizes an interval's ending time. Formulas describing how these times were related to the beginning and ending time of a corresponding WCR averaging interval are in the Appendix. Fig. 6b is a schematic of the first WCR averaging interval and Fig. 6d is a schematic of the second. Again, the subscripts "B" and "E" are used to indicate averaging beginning and ending times. Figures 6b and 6d both have lines at the top of an averaging interval/domain. The slopes of these lines are proportional to the ratio of two speeds. These speeds are a maximum likely snow particle speed toward the ground (v_p) and a horizontal wind advection speed (v_w). The v_p was calculated using averaged vertical-component Doppler velocities and v_w was calculated using a vertical profile of horizontal winds, based on WKA horizontal wind measurements and AF horizontal wind measurements (Figs. A1a-b), and using the WKA track vector (Table 2). An altitude (z' = 3400 m) was assumed in the calculation of v_w . This is the altitude of the ridges west and northwest of the HP site (Figs. 3a-b). Picking the altitude to be either z' = 3200 m or z' = 3600 m does not alter our findings.

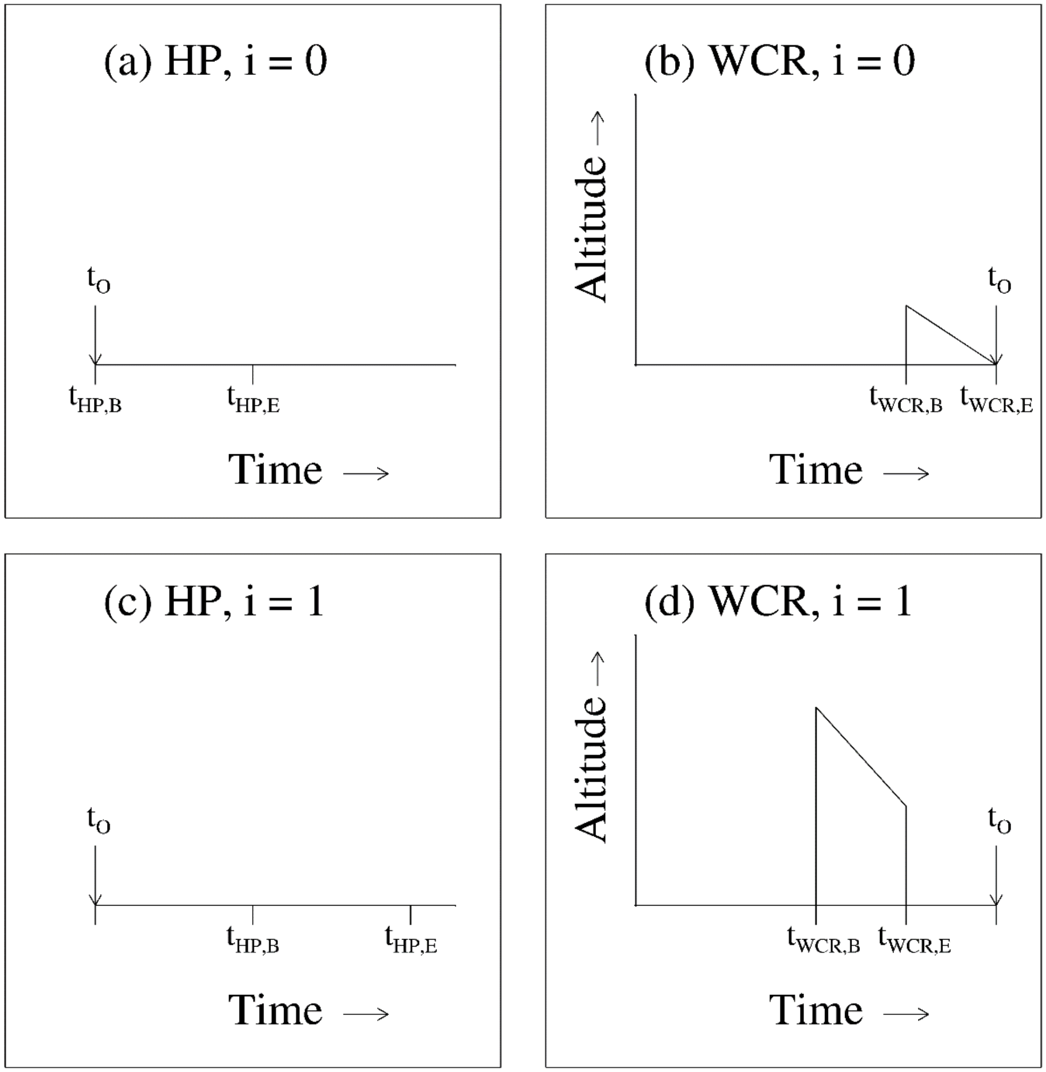

Figure 6 – (a and c) Representations of the $i = 0$ and $i = 1$ HP averaging intervals. (b and d) Representations of the $i = 0$ and $i = 1$ WCR averaging intervals/domains. The t_O is shown in all panels. The subscripts "B" and "E" indicate beginning and ending times of HP averaging (panels a and c) and the beginning and ending times of WCR averaging (panels b and d).

All panels in Fig. 6 are labeled with an index designating either the first averaging interval ($i = 0$) or the second averaging interval ($i = 1$) . Figures 7 and 8 present hotplate snowfall measurements from 14/15 December 2016 and 3 January 2017. In these, and in subsequent figures, colored circles surround the indexes, blue is used to color-code 15 December 2016, and red is used to color-code 3 January 2017.

Figures 9a-b and Figs. 10a-b have enlarged views of the altitude-time crossections recorded on the two flight days. Different from Fig. 5a and Fig. 5c, these measurements are only from the WCR's down-looking antenna. Additional differences are the following: 1) The plots are set up so that Z and V_D structures downwind of the hotplate can be seen. These structures are discussed in the following section. 2) The WCR measurements are shown for 50 s of flight. With the WKA ground speed approximately 125 m s^{-1} (Table 2), the distance along the abscissa is 6250 m. 3) Colored circles that surround the $i = 0$ index are placed below the WCR averaging intervals/domains. The latter are drawn with solid black lines and are seen to overlay both the Z and V_D altitude-time crossections. Consistent with Figs. 6b and 6d, and the Appendix, one of these black lines is vertical and the other is negatively sloped.

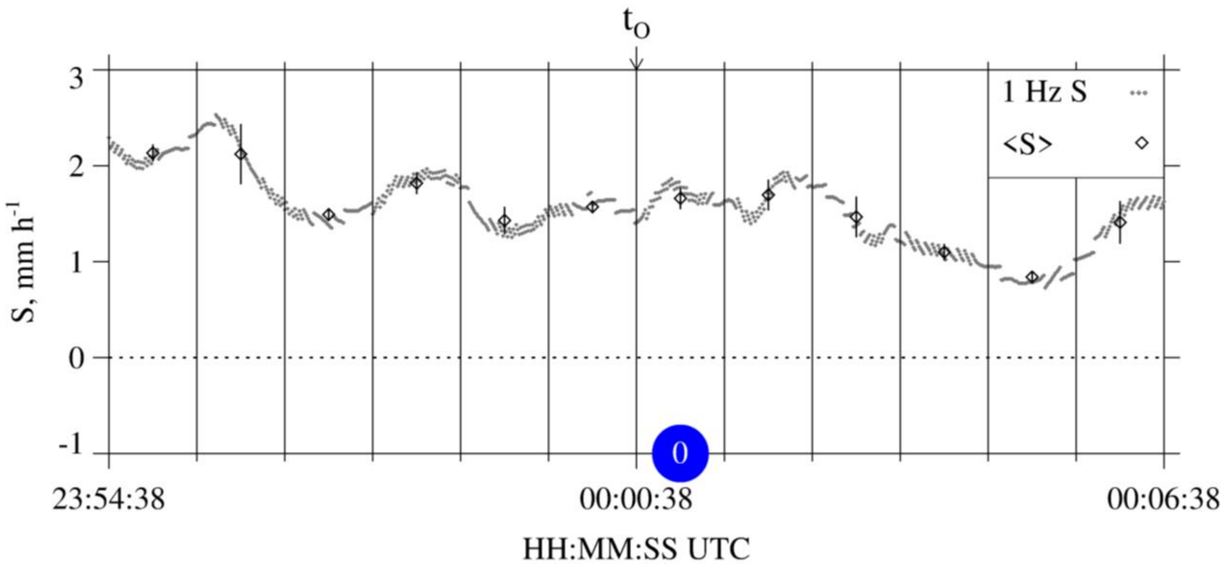

Figure 7 – Twelve minutes of HP snowfall measurements from 14/15 December 2016. Gray dots are S values calculated using hotplate output recorded at 1 Hz. Black diamonds are the one-minute-averaged values (± 1 standard deviation). The t_O is shown above the panel and the blue circle designates the $i = 0$ HP averaging interval.

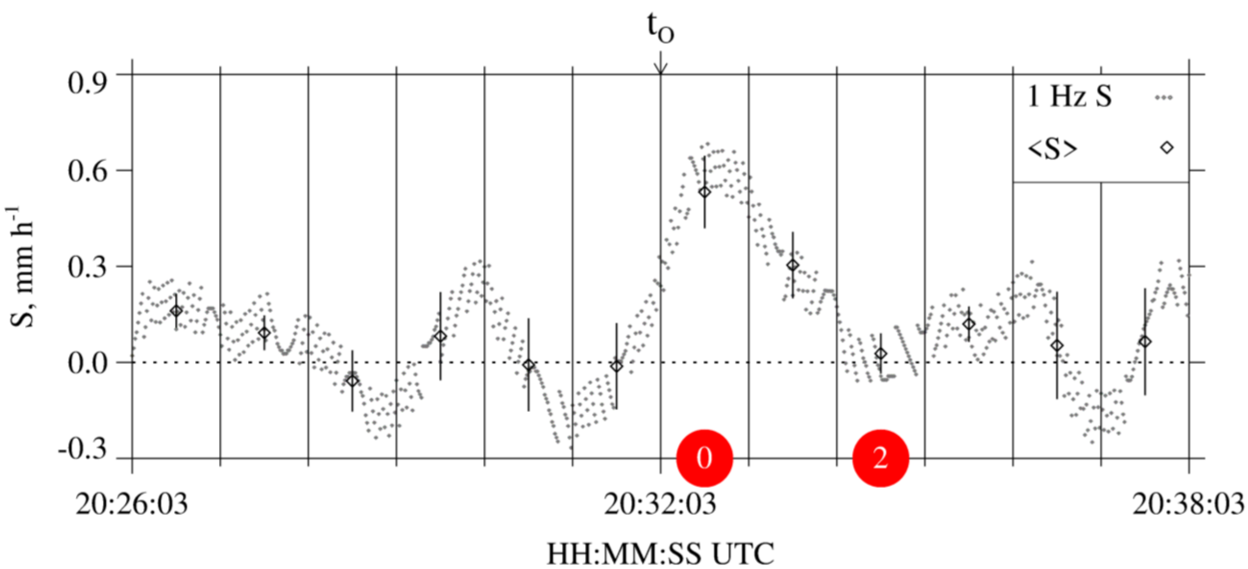

Figure 8 – Twelve minutes of HP snowfall measurements from 3 January 2017. Gray dots are S values calculated using hotplate output recorded at 1 Hz. Black diamonds are the one-minute-averaged values (± 1 standard deviation). The t_O is shown above the panel, a red circle designates the $i = 0$ HP averaging interval, and a red circle designates the $i = 2$ HP averaging interval.

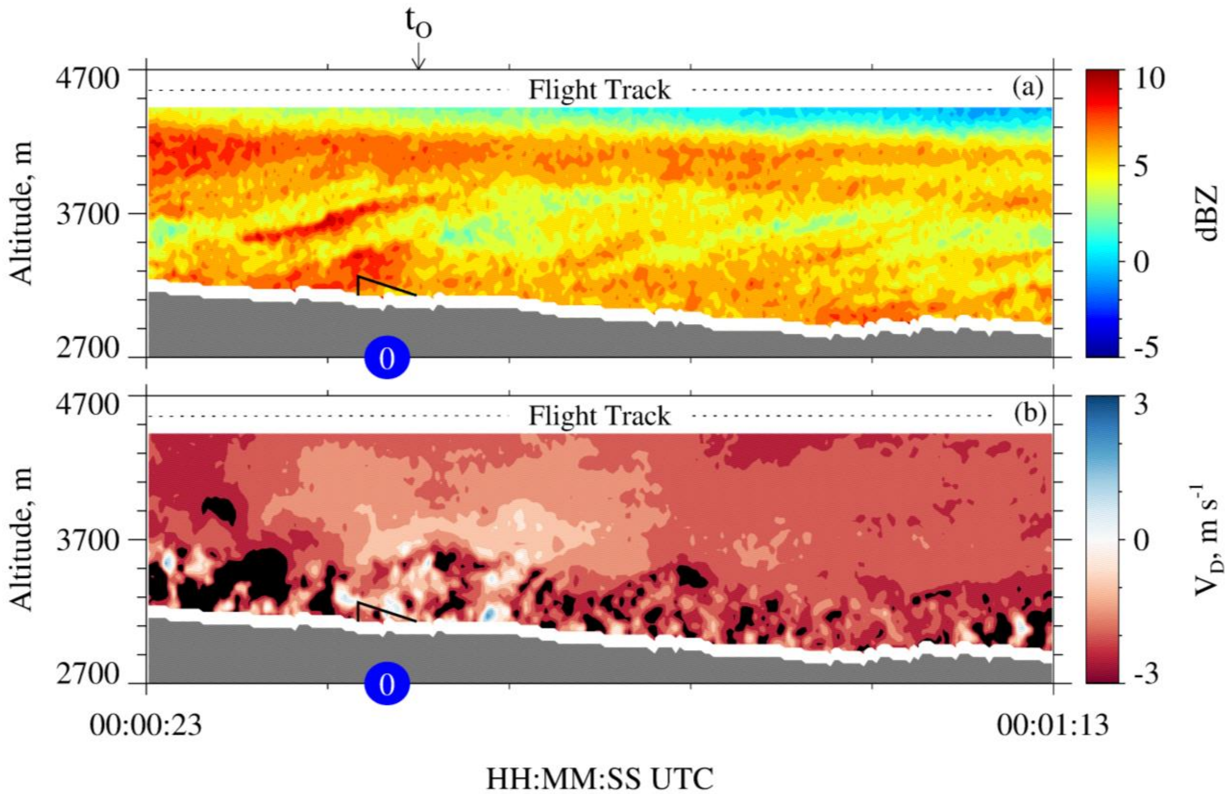

Figure 9 – 50 s of measurements from the down-looking WCR antenna on 15 December 2016. (a) Crossection of reflectivity t_O - 15 s to t_O + 35 s. (b) Crossection of Doppler velocity t_O - 15 s to t_O + 35 s. The t_O is shown above the top panel. In both panels, the solid black lines (vertical and sloped) encompass the $i = 0$ WCR averaging interval/domain and blue circles designate the $i = 0$ WCR averaging interval.

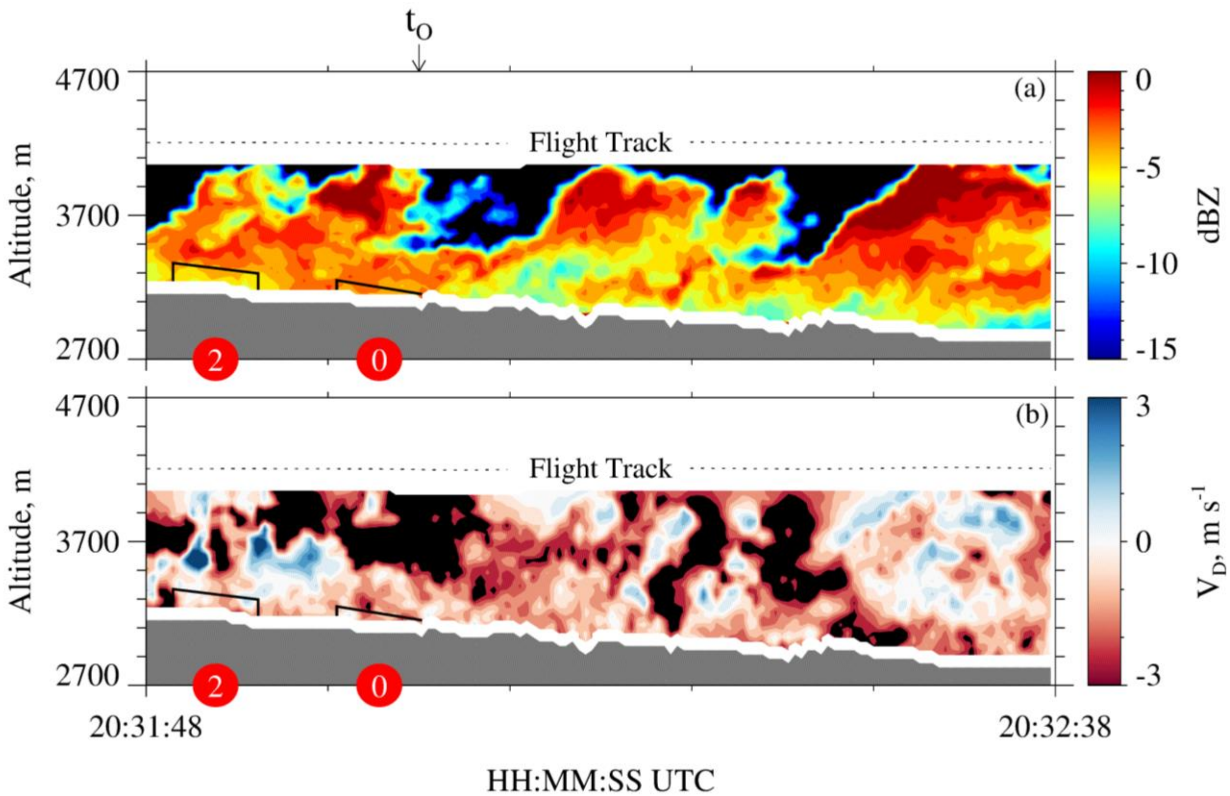

Figure 10 – 50 s of measurements from the down-looking WCR antenna on 3 January 2017. (a) Crossection of reflectivity t_o - 15 s to t_o + 35 s. (b) Crossection of Doppler velocity t_o - 15 s to t_o + 35 s. The t_o is shown above the top panel. In both panels, the solid black lines (vertical and sloped) encompass the $i=0$ and $i=2$ WCR averaging intervals/domains, two red circles designate the $i=0$ WCR averaging interval, and two red circles designate the $i=2$ WCR averaging interval.

The $i = 0$ averages of S and Z are presented in Table 5 and the corresponding averaging intervals are viewable in Fig. 7 and Fig. 9a (15 December 2016) and in Fig. 8 and Fig. 10a (3 January 2017). The $i = 1$ averages are also presented in Table 5. According to the averaging scheme (Fig. 6), the $i = 1$ HP averaging interval is time-shifted positively compared to the $i = 0$ HP averaging interval and the $i = 1$ WCR averaging interval is time-shifted negatively compared of the $i = 0$ WCR averaging interval. This arrangement of the averaging intervals is one way to average while also accounting for wind advection of the snow particles.

As discussed earlier in this section, the averaging scheme initializes with 60-second blocks of HP data between t_O and t_O +120 s. When we applied the scheme to data from 3 January 2017, but outside the specified time range, an inconsistency was documented. This is apparent in Fig. 8, where the t_O +120 s to t_O +180 s interval (i.e., the $i = 2$ interval) has negligible average S, while in Fig. 10, the $i = 2$ interval has a non-negligible average Z (~ 0.3 mm^6 m^{-3}). A firm explanation is not available for the inconsistency, but a factor may be the convective nature of the fields in Figs. 10a-b. Because of the inconsistency, only averages corresponding to the $i = 0$ and $i = 1$ intervals were analyzed further.

Table 5 – Averaged wind, hotplate, and WCR measurements

Date	v_w [a], m s^{-1}	i index	$\langle S \rangle \pm \sigma_S$ [b], mm h^{-1}	WCR Samples [c]	$\langle V_D \rangle$ [d], m s^{-1}	σ_{V_D} [e], m s^{-1}	v_p [f], m s^{-1}	$\langle Z \rangle \pm \sigma_Z$ [g], mm^6 m^{-3}
15 December 2016	7.4	0	1.7±0.1	42	-1.3	0.9	2.2	4.9±2.1
15 December 2016	7.4	1	1.7±0.2	149	-1.8	1.2	3.0	5.6±1.1
3 January 2017	8.9	0	0.5±0.1	22	-0.9	0.8	1.7	0.49±0.05
3 January 2017	8.9	1	0.3±0.1	35	-0.8	0.4	1.2	0.50±0.10

[a] Horizontal wind advection speed (Eq. A7) calculated using values from the penultimate and last columns of Table 2.

[b] One-minute average of the undercatch-corrected liquid-equivalent snowfall rate (± 1 standard deviation). An example averaging interval is the $i = 0$ interval in Fig. 7.

[c] Number of samples used to calculate WCR statistics in the penultimate four columns. The averaging intervals/domains (e.g., $i = 0$ in Figs. 9a-b and in Figs. 10a-b) encompass the averaged WCR samples.

[d] Average of Doppler velocity within the averaging intervals/domains.

[e] Standard deviation of Doppler velocity within the averaging intervals/domains.

[f] Maximum likely snow particle speed toward the ground (Eq. A8).

[g] Average reflectivity (± 1 standard deviation). These values are not corrected for attenuation.

3.6 - Snow Particle Imagery

In Fig. 9a and Fig. 10a, the time for a snow particle to move the abscissa and ordinate distances is different. The ratio of these two times is 2.6. This follows from our choice of abscissa and ordinate ranges, from values of particle fall speed (1 m s^{-1}) and horizontal wind advection speed (8 m s^{-1}), which we assumed, and from the WKA ground speed (gs ~ 125 m s^{-1}; Table 2). The assumed values are approximately consistent with values of $< V_D >$ and v_w , in Table 5, and with the V_D sign convention (Sect. 2.3). We also used $gs = 125$ m s^{-1} to scale (virtually) the time axes in Fig. 9a and Fig. 10a to a horizontal distance. Within the scaled coordinate frames, we assumed that all snow particle trajectories have negative slope ($\Delta z / \Delta x$ = -1 m s^{-1} / 8 m s^{-1} = -0.12) and that all trajectories are stationary. However, both assumptions seem inconsistent with the reflectivity structures in Fig. 5a, where positively-sloped particle fall streaks are evident at ~ 5500 m, inconsistent with Fig. 9a where positively-sloped fall streaks are at ~ 3500 m, and inconsistent with the positively-sloped fall streaks in Fig. 10a. On both flight days, the fall streaks evince particle sources that move horizontally and with a horizontal speed that is larger than the v_w = 8 m s^{-1} applied in the estimate of the trajectory slope. It may be that the source's horizontal speed is comparable to the flight-level WKA-derived horizontal wind (27 to 32 m s^{-1}; Table 2) but we do not have data needed to verify that assertion. Based on the assumption that snow particles followed the fall streaks while both were advecting horizontally, we looked *downwind* of the hotplate - at a time later than t_O in Fig. 9a and Fig. 10a - for particles that became those that produced snowfall at the hotplate.

Particle images from 15 December 2016 were analyzed using the 2DP. With this instrument the maximum all-in particle size (in the horizontal direction perpendicular to flight) is

6400 μm and the particle size resolution is 200 μm (Sect. 2.2). Within the time interval picked for this analysis (discussed below), particles sizing in the smaller of the two spectral modes, with mode size ~ 400 μm, were more numerous (results not shown). Because the 400 μm particles are poorly resolved by the 2DP, and the same can be said for somewhat larger particles, those smaller than 1000 μm were excluded from the following analysis. Figure 11a shows imagery from 12 s of measurements acquired near the end of the sequence in Fig. 9a (00:01:02 to 00:01:14). This time interval was selected by tracing forward from t_o, along the slope of the fall streaks, to the flight level. Many of the particles are rounded (indicating riming) and a few have arms likely due to incomplete conversion of branched crystals to rimed snow particles. The mode size corresponding to these images is 1600 μm. No liquid water was detected with these particles (LWC < 0.01×10^{-3} kg m^{-3}; Fuller 2020; her Figure 8), but liquid was detected, at ~ 00:00:00, as the aircraft approached the ridgeline (Figs. 5a-b).

Turning to imagery from 3 January 2017, the most appropriate location for analysis would be through the second billow structure evident in Fig. 10a. This billow sourced a fall streak that terminated at the hotplate (i.e., at the time t_o indicated in the figure). However, the aircraft only clipped the top of this billow, and it was only when sampling the billow seen ~ 13 s earlier that larger ice particle concentrations (~ 20,000 m^{-3}) (Fuller 2020; her Figure 10) and larger LWC (~ 0.08×10^{-3} kg m^{-3}; Fig. 5d) were detected. Maximum reflectivities were the same in all three billows (Z ~ 1 mm^6 m^{-3}; 0 dBZ), so it was assumed that imagery collected in the first billow (20:32:00 to 20:32:02) was representative of what was falling toward the hotplate. The 2DS was used to image these particles (Fig. 11b); with this instrument the maximum all-in particle size (in the horizontal direction perpendicular to flight) is 1280 μm and the size resolution is 10 μm (Sect. 2.2). Most of the objects in Fig. 11b appear to be rimed and their mode size is ~ 400 μm. It is also noted that particles smaller than 100 μm were eliminated from these images, however, compared to the ~ 400 μm particles those smaller than 100 μm were significantly less abundant (results not shown).

(a)

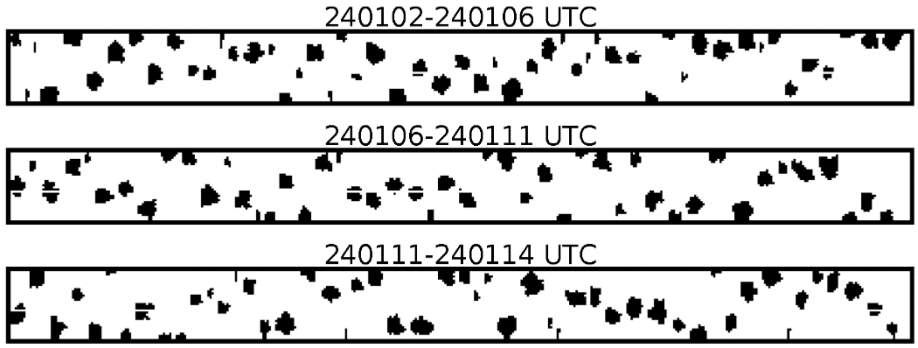

(b)

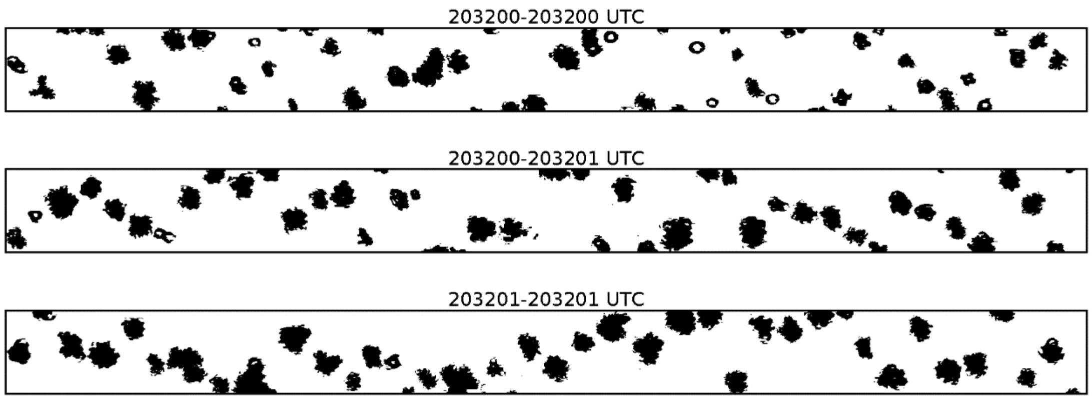

Figure 11 – (a) 2DP particle imagery from 15 December 2016. The height of the strips is 6400 μm. These particles are estimated to be representative of those that fell from flight level toward the hotplate. (b) 2DS particle imagery from 3 January 2017. The height of the strips is 1280 μm. These particles are estimated to be representative of those that fell from flight level toward the hotplate.

3.7 – S/Z Relationships

Our S/Z pairs are presented in Table 5 where the indexes ($i = 0$ and $i = 1$) are used to indicate results derived for the averaging intervals. Here, the reflectivities are not corrected for attenuation, however, in Fig. 12, the attenuation-corrected reflectivities are plotted. Uncorrected-reflectivities from Table 5, attenuations from Table 3, and Eq. 1 were used to calculate the corrected reflectivities. Also shown is a subset of the S/Z pairs from PV11's Fig. 11 (0.01 < Z < 10 mm^6 mm^{-3}) and the PV11 best-fit line (black). In the figure legend, results from PV11 are specified as S(ρ_1)/Z because those authors applied the lower of two density-size functions (ρ_1) with airborne measurements of optical particle images to calculate the snowfall rates (Sect. 1). Our data pairs plot above the S(ρ_1)/Z line but within the variability of PV11's measurements.

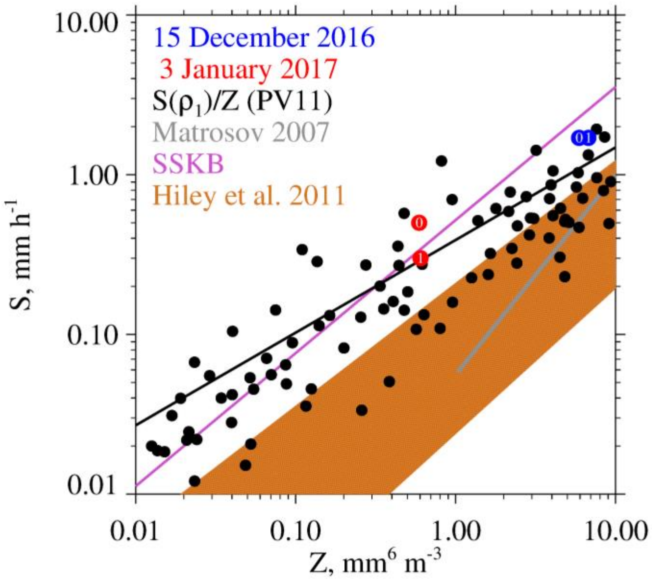

Figure 12 – Snowfall rate versus radar reflectivity. Colored circles indicate attenuation-corrected reflectivities (Table 3, Table 5, and Eq. 1) for the $i = 0$ and $i = 1$ averaging intervals. The $S(\rho_1)/Z$ points are a subset from PV11's Fig. 11 ($0.01 < Z < 10$ mm^6 mm^{-3}). Also plotted is the PV11 best-fit line (black), the S/Z relationship from Matrosov (2007), the S/Z relationship abbreviated SSKB (Sect. 1), and the swath of S/Z relationships, for crystals, from Hiley et al. (2011).

There are two potential biases in the values of S we tabulate (Table 5) and plot (Fig. 12). First, the two snowfall events had flight-level vertical wind velocities that were positive (upward) upwind of the summit, and vice versa downwind of the summit. Except for the strongest downdraft on 3 January 2017, the magnitude of this variance is ~ 1 m s^{-1} (Figs. 5b and 5d). Assuming 1 m s^{-1} was the downward wind immediately over the hotplate, the snow particles would have approached the gauge faster than their fall speed, and especially so on 3 January 2017. Our basis for stating this is fall speeds for the mode sizes discussed in Sect. 3.6 (1600 and 400 μm) and our assumption that the particles were graupel. (Table 6 has these characteristic sizes and fall speeds.) However, the conjectured downdraft speed is likely an overestimate - because of divergence occurring as the draft approached the surface - and because the sizes in Table 6 likely underestimate what fell to the hotplate. Relevant to the last of these assertions, we used the T/RH/altitude measurements (Table 2) to calculate the vertical distance available for growth via riming, and thus for a fall speed increase, between the flight level and the lifted condensation level. Assuming an adiabatically-stratified liquid cloud and unit collection efficiency (these assumptions overestimate growth by riming), and no change of particle crossection (underestimates growth by riming), our calculations indicate that relative increases of size and fall speed were 40 and 20 %, respectively, on 3 January 2017, and that these relative increases were a factor-of-two larger on 15 December 2016.

Table 6 – Estimates of snow particle fall speed

Date	Mode Size, μm	Assumed Particle Type	Fall Speed, m s^{-1}	Reference
15 December 2015	1600	graupel	1.4	PV11; assuming ρ_1 in their Figure 5
3 January 2016	400	graupel	0.7	PV11; assuming ρ_1 in their Figure 5

Second, there is concern that values of S from 3 January 2017 are underestimated. Although, values of S must be > 0, we presented 1 Hz values (gray points, Fig. 8) approaching -0.3 mm h^{-1}. Negative values resulted because we did not impose a threshold of 0 mm h^{-1} on the uncorrected snowfall rates (this thresholding is discussed in Z18) and because negative snowfall rate values (uncorrected for catch inefficiency) are amplified by the gauge-catch correction (Sect. 2.4). The implication is that 0.2 mm h^{-1} could be added to the one-minute averaged values of S in Table 5 and in Fig. 12. Here, the assumption is that an averaged S of -0.2 mm h^{-1}, in Fig. 8, is indicating no snowfall at the hotplate; however, because the hotplate was operated autonomously (Sect. 2.1) we have no way to verify the assumption.

4 – Results

Figure 12 shows our S/Z measurements after we corrected the reflectivities for attenuation. Below we compare our S/Z measurements to calculations reported by Hiley et al. (2011), but first, we consider the computational S/Z relationship reported by Matrosov (2007) and its relevance to our measurements. Since the particle images (Figs. 11a-b) reveal no compelling evidence for the aggregates modeled by Matrosov (2007), a model based on that particle type is not a useful comparator. Moreover, the overlap of PV11's S/Z measurements and Matrosov's S/Z calculations has already been discussed in the literature (PV11). However, before going forward, two clarifications will be made about PV11's data points in Fig. 12: 1) Presentation clarity was what guided our selection of the S and Z axis ranges in this figure but with the consequence that 32 of PV11's S/Z pairs are not shown at Z > 10 mm^6 m^{-3}. 2) The scatter of PV11 data at the largest values of Z in Fig. 12, combined with the fact that PV11 points at Z > 10 mm^6 m^{-3} are not shown, could lead to the interpretation that the slope describing the relationship at Z approximately > 2 mm^6 m^{-3} should be decreased relative to the slope of the PV11 best-fit line. Readers who view PV11's Fig. 11 will conclude that this interpretation is not warranted.

Calculated S/Z relationship have inputs from parameterized descriptions of density, shape, fall speed, and PSD. The analysis conducted by Hiley et al. (2011) is the most comprehensive in this regard, and except for the one aggregate particle type those authors considered, out of 20 total, they modeled ensembles of crystals. Additionally, Hiley et al. (2011) did not model ensembles of spherical snow particles. The latter were modeled by Surussavadee and Staelin (2007) and Kulie and Bennartz (2009), and in Fig. 12 we are using SSKB to symbolize that computational approach (Sect. 1).

Departures between our S measurements (Fig. 12) and S/Z calculations from Hiley et al. (2011) were evaluated as the vertical distance between the top of the orange region and our S/Z data points. Reflectivities at the top of the orange region were calculated using attenuation-corrected reflectivities (Eq. 1 and Table 5) and the upper-limit S/Z equation from Hiley et al. (2011) ($S = 0.21 \cdot (Z')^{0.77}$; Sect. 1). The departures were evaluated as a relative difference expressed as $(S_{HP}-S)/S$ with S_{HP} one of four snowfall rates from Table 5. The relative difference is no smaller than 0.9 and 1.1 on 15 December and 3 January, respectively. These minimum relative differences exceed the hotplate precision (Sect. 2.4) by approximately a factor of three. We therefore conclude that our paired values of surface-measured precipitation rate and aircraft-measured radar reflectivity, after correcting for attenuation, provide evidence that a calculation of S based on the Hiley et al. (2011) upper-limit, when applied to rimed snow particles, is associated with a low-biased estimate of S.

A plausible explanation for the low bias is the smaller density implicit in most computationally-based S/Z relationships and especially those which assume that snow particles are crystals. Densities are quite different for crystals versus that for rimed snow particles. For example, in Kulie and Bennartz (2009; their Eq. 2), assuming a 2 mm crystal, the density is ~ 40 kg m^{-3}, whereas in PV11, assuming a 2 mm graupel particle, the density is ~ 200 kg m^{-3}. Fig. 12 also has the SSKB relationship. This was developed using density = 200 kg m^3 (Sect. 1). Compared to S/Z relationship represented by top of the orange region in Fig. 12, the SSKB line plots closer to our data points and closer to most of those reported by PV11.

Our conclusion that the upper-limit S/Z relationship from Hiley et al. (2011) underestimates S would be modified if the WCR-derived reflectivities were negatively biased.

Assuming the reflectivities are negatively biased by 2.5 dBZ, the minimum relative differences discussed previously are no smaller than 0.2 and 0.4 on 15 December and 3 January, respectively. A negative bias of this magnitude cannot be ruled out but neither can a positive bias of the same magnitude (Sect. 2.3). The latter increases the minimum relative differences to 1.9 and 2.3 on 15 December and 3 January, respectively.

The scatter of measurements in Figure 12, and the plausibility of a -2.5 to +2.5 dBZ bias in WCR reflectivity measurements, indicate that refined techniques will be needed for future investigations. Additionally, improved methods are needed to diagnose situations where riming is occurring within clouds. Both lidars and radiometers can sense supercooled liquid water from space (e.g., Battaglia and Panegrossi, 2020), and if combined with Doppler radar, can diagnose precipitation attributable to rimed snow particles. These approaches are being tested in ground-based field studies (Kneifel et al. 2015; Moisseev et al. 2017; Mason et al. 2018).

5 - Conclusions

This study is significant because it brings together direct measurements of snowfall rate, measured at the ground, and measurements of reflectivity from an airborne W-band radar. As shown in Fig. 12, our observations do not depart strongly from the PV11 best-fit line; however, they do plot somewhat larger. This excess could be consistent with downslope flow that occurs in lee of the Medicine Bow Mountains (Figs. 5a and 5d) or with calculations which indicate that larger density is associated with larger S, in the S-versus-Z coordinate system (PV11), combined with the intrinsic variability of rime ice (Macklin 1962).

If the downslope flow hypothesis is correct, and the PV11 best-fit line is applied to retrieve S in settings with rimed snow particles, we expect a negatively-biased S retrieval leeward of a ridgeline, and a positively-biased retrieval windward of a ridgeline. This follows because PV11 did not account for the effect of vertical air motion on their S/Z relationship, because of how vertical air motion changes windward to leeward across the Medicine Bow Mountain ridgeline (Figs. 5b-5d), and because the magnitudes of the windward/leeward vertical winds are comparable to the downward speed of rimed snow particles in quiescent air. Analysis of existing data, for example from the SNOWIE project that deployed in western Idaho in 2017 (Tessendorf et al. 2019), could further explore the hypothesis.

New research can also refine the S/Z relationship for rimed snow particles. This could be computational – exploring the utility of parameterizing S in terms of both Z and density – or could be observational. Unlike the investigation of PV11, where only an airborne platform was employed, we have demonstrated how useful information can be obtained with ground-based and airborne systems. Another approach would be with collocated ground-based instrumentation, for density and particle imaging, and for measuring wind, snowfall rate, and radar reflectivity. This would avoid some of the complications encountered in this study, including W-band attenuation and a reliance on particle imagery acquired aloft. A close-range measuring radar might also allow retrievals closer to the surface than in this work. Improvement of methods that remotely sense supercooled cloud water are also needed.

6 - Appendix

This appendix explains how HP (hotplate) and WCR (Wyoming Cloud Radar) averages were evaluated. The scheme starts with an HP averaging interval (duration 60 s) and derives a WCR averaging interval and a WCR averaging domain. The latter encompasses a subset of the altitude-time crossection sampled by the WCR. The top boundary of the domain was derived using vertical-component Doppler velocities within the interval/domain. Because of this dependence, the line defining the top boundary was derived iteratively.

With the overflight time symbolized t_O, the beginning and ending times of the first of two 60-second HP averaging intervals are

$$t_{HP,B} = t_O \tag{A1}$$

$$t_{HP,E} = t_O + 60 \tag{A2}$$

Since two adjacent HP averaging intervals are evaluated in this analysis, we express the averaging times with the following recursive equations

$$t_{HP,B}\left(i\right) = t_O + i \cdot 60 \tag{A3}$$

and

$$t_{HP,E}\left(i\right) = t_O + (i+1) \cdot 60 . \tag{A4}$$

In Eqs. A3-A4 the index is $i \in \{0, 1\}$.

Analogous to the recursion in Eq. A4, the ending time of a WCR averaging interval is

$$t_{WCR,E}\left(i\right)=t_O-i\cdot 60\cdot v_w/gs\ . \qquad \text{(A5)}$$

Here v_w is a wind advection speed (discussed below) and the second term on the rhs is a wind advection distance divided by the WKA (Wyoming King Air) ground speed (gs). Analogous to the Eq. A5, the beginning time of a WCR averaging interval is

$$t_{WCR,B}\left(i\right)=t_{WCR,E}-(i+1)\cdot 60\cdot v_w/gs \qquad \text{(A6)}$$

The wind advection speed (v_w) in Eqs. A5-A6 was calculated using an altitude-dependent west-to-east wind velocity (u) and an altitude-dependent south-to-north wind velocity (v). These altitude-dependent component velocities were calculated using the horizontal wind vectors in the penultimate and last columns of Table 2. Plots of the component velocities versus altitude and the linear functions used to relate component velocities to altitude are presented in Figs. A1a-b.

An altitude (z' = 3400 m) was assumed for evaluating the horizontal wind advection vector. This is the altitude of the ridges west and northwest of the HP site (Figs. 3a-b).

The WKA track vector (Table 2) defines the vertical plane of the WCR measurements. We assumed that wind advection of snow particles occurred parallel to this vector. With the assumption stated in the previous paragraph, the horizontal wind advection speed (v_w) was calculated as the projection of the horizontal wind vector onto the track vector.

$$v_w=\frac{u\left(z'\right)\cdot gs_x+v\left(z'\right)\cdot gs_y}{\left(gs_x^2+gs_y^2\right)^{1/2}} \qquad \text{(A7)}$$

In Eq. A7 the west-to-east and south-to-north components of the track vector are symbolized gs_x and gs_y. Vector representations of the track vector are in Table 2. On 14/15 December 2016 and 3 January 2017, the values of v_w are 7.4 and 8.9 m s^{-1}, respectively.

In addition to the properties gs and v_w used to evaluate Eqs. A5-A6, a WCR averaging interval/domain was evaluated using a snow particle downward speed (Eq. A8).

$$v_p = |<V_D>| + \sigma_{V_D} \qquad \text{(A8)}$$

Here, $<V_D>$ is the average of Doppler velocities within an averaging interval/domain, $|<V_D>|$ is the absolute value of the average, and σ_{V_D} is the standard deviation of the average. On both the lhs and rhs of Eq. A8, all terms are greater than zero.

We interpret v_p as the maximum likely snow particle speed toward the ground. There are three reasons for this: 1) For the WCR averaging intervals/domains we analyzed, values of $<V_D>$ were consistently less than zero. This indicates that snow particles (on average) were moving toward the ground. 2) Again, for the WCR averaging intervals/domains we analyzed, σ_{V_D} was comparable to $|<V_D>|$. This indicates that turbulent eddies transported snow particles upward and downward at a speed comparable their downward speed in quiescent air. 3) The V_D are reflectivity weighted (Haimov and Rodi 2013) and are thus indicative of the motion of the largest particles within an averaging interval/domain.

We now focus on the top boundary of a WCR averaging interval/domain. Figures 6b and 6d have representations of the boundary. The slope defining this boundary was calculated as $-v_p \cdot gs / v_w$. That is, particles below this boundary moved downward sufficiently fast and horizontally sufficiently slow to advect reasonably close to the hotplate. Starting with diagnosed values of gs and v_w, the values of v_p and slope, were derived iteratively. The precision of the derived v_p is ± 0.1 m s^{-1}.

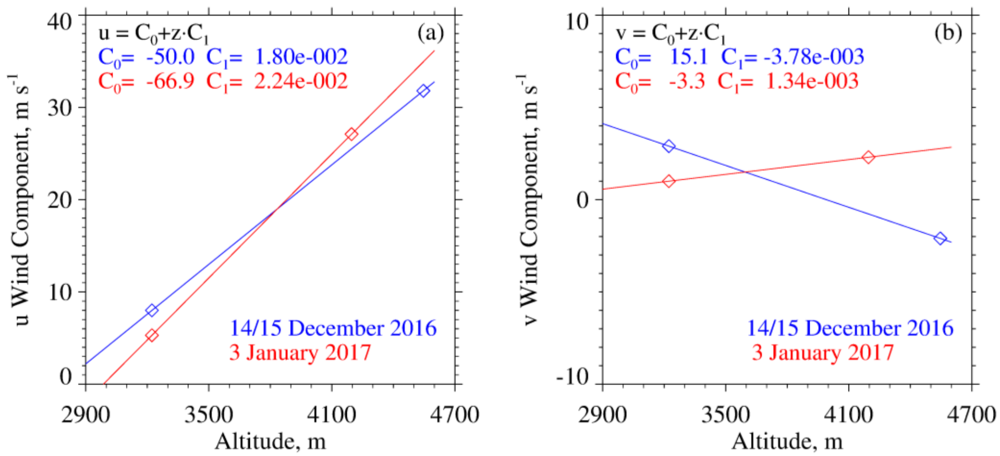

Figure A1 – (a) West-to-east (u) wind velocity derived using measurements from the WKA and the AmeriFlux (AF) tower. Also shown is the linear function used to relate u to altitude. (b) South-to-north (v) wind velocity derived using measurements from the WKA and AF. Also shown is the linear function used to relate v to altitude. WKA and AF velocities are presented as vectors in the penultimate and last columns of Table 2.

Data Availability. The WKA and WCR measurements can be obtained from the SNOWIE data archive of NCAR/EOL, which is sponsored by the National Science Foundation. Hotplate gauge measurements are at https://doi.org/10.15786/20103146. The US-GLE AmeriFlux measurements are at https://ameriflux.lbl.gov/. The Brooklyn Lake SNOTEL gauge measurements are at https://www.wcc.nrcs.usda.gov/snow/. Merged Hotplate, SNOTEL, and AmeriFlux data sequences from 14/15 December 2016 and 3 January 2017 are in Snider (2023).

Author contributions. JS and MB wrote the grant proposal that funded this research. Field measurements were performed by SF, SM, SH, MB, and JS. SF wrote her MS dissertation, and this was adapted for this paper by JS. KS processed the snow particle imagery. AM maintained the measurement sites. All authors contributed to the editing of this paper.

Acknowledgements –

We acknowledge the expert technical assistance provided by David Plummer, Larry Oolman, Zane Little, Brent Glover, Edward Sigel, Thomas Drew, and Brett Wadsworth. We thank SNOWIE project PI Jeffery French, who provided the flight data, Gabor Vali who provided the S/Z data points in Figure 12, and John Frank and John Korfmacher who acquired the GLE-US AmeriFlux data set. This work was supported by the United States National Science Foundation (Award Number 1850809) and the John P. Ellbogen Foundation.

References

AmeriFlux, https://ameriflux.lbl.gov/, 2021

Battaglia, A. and Panegrossi, G., What Can We Learn from the CloudSat Radiometric Mode Observations of Snowfall over the Ice-Free Ocean?, 12, 3285, https://doi.org/10.3390/rs12203285, 2020

Boudala, F.S., R. Rasmussen, G.A. Isaac, and B. Scott, Performance of Hot Plate for Measuring Solid Precipitation in Complex Terrain during the 2010 Vancouver Winter Olympics, J. Atmos. Oceanic Technol., 31, 437–446, https://doi.org/10.1175/JTECH-D-12-00247.1, 2014

Braham , R. R., Snow Particle Size Spectra in Lake Effect Snows. J. Appl. Meteor. Climatol., 29, 200–207, https://doi.org/10.1175/1520-0450(1990)029<0200:SPSSIL>2.0.CO;2, 1990

Brock, F. V., and Richardson, S. J., Meteorological Measurement Systems, Oxford University Press, New York, 304 pp., 2001

Cocks, S.B., S.M. Martinaitis, B. Kaney, J. Zhang, and K. Howard, MRMS QPE Performance during the 2013/14 Cool Season, J. Hydrometeor., 17, 791–810, https://doi.org/10.1175/JHM-D-15-0095.1, 2016

Faber, S., French, J. R., and Jackson, R., Laboratory and in-flight evaluation of measurement uncertainties from a commercial Cloud Droplet Probe (CDP), Atmos. Meas. Tech., 11, 3645–3659, https://doi.org/10.5194/amt-11-3645-2018, 2018

Field, P.R., Hogan, R.J., Brown, P.R.A., Illingworth, A.J., Choularton, T.W. and Cotton, R.J., Parametrization of ice-particle size distributions for mid-latitude stratiform cloud. Q.J.R. Meteorol. Soc., 131: 1997-2017. https://doi.org/10.1256/qj.04.134, 2005

Fuller, S.E., Improvement of the Snowfall / Reflectivity Relationship for W-band Radars, MS Thesis, Department of Atmospheric Science, University of Wyoming, 2020

Geerts, B., Q. Miao, Y. Yang, R. Rasmussen, and D. Breed, An Airborne Profiling Radar Study of the Impact of Glaciogenic Cloud Seeding on Snowfall from Winter Orographic Clouds, J. Atmos. Sci., 67, 3286–3302, https://doi.org/10.1175/2010JAS3496.1, 2010

Haimov, S., and Rodi, A., Fixed-Antenna Pointing-Angle Calibration of Airborne Doppler Cloud Radar, Journal of Atmospheric and Oceanic Technology, 30, 2320-2335, https://doi.org/10.1175/JTECH-D-12-00262.1, 2013

Hiley, M. J., M. S. Kulie, and R. Bennartz, Uncertainty Analysis for CloudSat Snowfall Retrievals, J. Appl. Meteor. Climatol., 50, 399–418, 2011

Kneifel, S., von Lerber, A., Tiira, J., Moisseev, D., Kollias, P., and Leinonen, J., Observed relations between snowfall microphysics and triple-frequency radar measurements. J. Geophys. Res. Atmos., 120, 6034– 6055, doi: 10.1002/2015JD023156, 2015

Kochendorfer, J., Nitu, R., Wolff, M., Mekis, E., Rasmussen, R., Baker, B., and Jachcik, A, Testing and development of transfer functions for weighing precipitation gauges in WMO-SPICE, Hydrology and Earth System Sciences, 2, 1437-1452, https://doi.org/10.5194/hess-22-1437-2018, 2018

Korolev, A. V., E. F. Emery, J. W. Strapp, S. G. Cober, G. A. Isaac, M. Wasey, and D. Marcotte, Small ice particles in tropospheric clouds: Fact or artifact? Airborne Icing Instrumentation Evaluation Experiment, Bull. Amer. Meteor. Soc., 92, 967–973, https://doi.org/10.1175/2010BAMS3141.1, 2011

Kulie, M. S., and R. Bennartz, Utilizing Spaceborne Radars to Retrieve Dry Snowfall, J. Appl. Meteor. Climatol., 48, 2564–2580, https://doi.org/10.1175/2009JAMC2193.1, 2009

Kulie, M. S., Milani, L., Wood, N. B., Tushaus, S. A., Bennartz, R., and L’Ecuyer, T. S., A Shallow Cumuliform Snowfall Census Using Spaceborne Radar, Journal of Hydrometeorology, 4, 1261-1279, https://doi.org/10.1175/JHM-D-15-0123.1, 2016

Lawson, R. P., O’Connor, D., Zmarzly, P., Weaver, K., Baker, B., Mo, Q., and Jonsson, H., The 2D-S (Stereo) Probe: Design and Preliminary Tests of a New Airborne, High-Speed, High-Resolution Particle Imaging Probe, J. Atmos. Ocean. Tech., 23, 1462–1477, https://doi.org/10.1175/JTECH1927.1, 2006

Liebe, H.J., Manabe, T., and Hufford, G.A., Millimeter–wave attenuation and delay rates due fog/cloud conditions, IEEE Trans. Antenn. Propag., 37, 1617–1623, 1989

Locatelli, J.D. and Hobbs, P.V., Fall speed and masses of solid precipitation particles, J. Geophys. Res., 79, 2185–2197, https://doi.org/10.1029/JC079i015p02185, 1974

Macklin, W.C., The density and structure of ice formed by accretion, Q.J.R.Meteorol.Soc., 88: 30-50. doi:10.1002/qj.49708837504, https://doi.org/10.1002/qj.49708837504, 1962

Marlow, S.A, J.M. Frank, M. Burkhart, B. Borkhuu, S.E. Fuller, and J.R. Snider, Snowfall measurements in mountainous terrain, in revision for the Journal of Applied Meteorology and Climatology, http://www-das.uwyo.edu/~jsnider/JAMC-D-22-0093_6.pdf, 2023

Martinaitis, S.M., S.B. Cocks, Y. Qi, B.T. Kaney, J. Zhang, and K. Howard, Understanding winter precipitation impacts on automated gauge observations within a real-rime system, J. Hydrometeor., 16, 2345-2363, https://doi.org/10.1175/JHM-D-15-0020.1, 2015

Mason, S. L., Chiu, C. J., Hogan, R. J., Moisseev, D., and Kneifel, S., Retrievals of riming and snow density from vertically pointing Doppler radars, Journal of Geophysical Research: Atmospheres, 123, 13,807– 13,834, https://doi.org/10.1029/2018JD028603, 2018

Matrosov, S.Y., Modeling Backscatter Properties of Snowfall at Millimeter Wavelengths, J. Atmos. Sci., 64, 1727-1736, https://doi.org/10.1175/JAS3904.1, 2007

Moisseev, D., von Lerber, A., and Tiira, J., Quantifying the effect of riming on snowfall using ground-based observations, J. Geophys. Res. Atmos., 122, 4019–4037, doi:10.1002/2016JD026272, 2017

Nemarich, J., Wellman, R.J., and Lacombe, J., Backscatter and attenuation by falling snow and rain at 96, 140, and 225 GHz, IEEE Trans. Geosci. Remote, 26, 319–329, 1988

Panofsky, H.A. and Dutton, J.A., Atmospheric Turbulence, Wiley-Interscience, New York, 397 pp., 1984

Pokharel, B. and G. Vali, Evaluation of Collocated Measurements of Radar Reflectivity and Particle Sizes in Ice Clouds, J. Appl. Meteor. Climatol., 50, 2104–2119, https://doi.org/10.1175/JAMC-D-1005010.1, 2011

Rasmussen, R.M., J. Hallett, R. Purcell, S.D. Landolt, and J. Cole, The Hotplate precipitation gauge, J. Atmos. Oceanic Technol., 28, 148-164, https://doi.org/10.1175/2010JTECHA1375.1, 2011

R.M. Young Company, Model 05103 Wind Monitor, 2001

Serreze, M. C., M. P Clark, and R. L. Armstrong, D. A. MacGinnis, and R. S. Pulwarty, Characteristics of the western United States snowpack from snowpack telemetry (SNOTEL) data, Water Resources Research, 35, 2145-2160, https://doi.org/10.1029/1999WR900090, 1999

Skofronick-Jackson, G., and Coauthors, The Global Precipitation Measurement (GPM) Mission for science and society, Bull. Amer. Meteor. Soc., 98, 1679–1695, https://doi.org/10.1175/BAMS-D-15-00306.1, 2017

Smith, P.L., Equivalent radar reflectivity factors for snow and ice particles, J. Climatol. Appl. Meteor., 23, 1258–1260, https://doi.org/10.1175/1520-0450(1984)023<1258:ERRFFS>2.0.CO;2, 1984

Snider, J.R., Supplemental dataset for Marlow et al. (2023), https://doi.org/10.15786/20247870, 2023

Surussavadee, C., and D. H. Staelin, Millimeter-Wave Precipitation Retrievals and Observed-versus-Simulated Radiance Distributions: Sensitivity to Assumptions. J. Atmos. Sci., 64, 3808–3826, https://doi.org/10.1175/2006JAS2045.1, 2007

Tessendorf, S. A., and Coauthors, A transformational approach to winter orographic weather modification research: The SNOWIE Project, Bulletin of the American Meteorological Society, 100, 71–92, https://doi.org/10.1175/BAMS-D-17-0152.1, 2019

Ulaby, F.T., Moore, R.K., and Fung, K., Microwave Remote Sensing: Active and Passive, vol 2, Addison–Wesley, Advanced Book Program, Reading, MA, p. 456., 1981

Vaisala, User's Guide, Vaisala Weather Transmitter, WXT520, 2012

Vali, G. and Haimov, S., Observed extinction by clouds at 95 GHz, IEEE Trans. Geosci. Remote, 39, 190–193, 2001

Wang, P.K., and W. Ji, Collision Efficiencies of Ice Crystals at Low–Intermediate Reynolds Numbers Colliding with Supercooled Cloud Droplets: A Numerical Study, Journal of the Atmospheric Sciences, 57, 1001-1009, https://doi.org/10.1175/1520-0469(2000)057<1001:CEOICA>2.0.CO;2, 2000

Wilson, J., and E. Brandes, Radar measurement of rainfall—A summary, Bull. Amer. Meteor. Soc., 60, 1048–1058, https://doi.org/10.1175/1520-0477(1979)060<1048:RMORS>2.0.CO;2, 1979

Wolfe, J.P., and J.R. Snider, A relationship between reflectivity and snow rate for a high-altitude S-band radar, J. Appl. Meteor. Climatol., 51, 1111–1128, https://doi.org/10.1175/JAMC-D-11-0112.1, 2012

Young, H.D., Statistical Treatment of Experimental Data, pp. 172, McGraw-Hill, New York, 1962

Zaremba, T.J., and Coauthors, Vertical motions in orographic cloud systems over the Payette River Basin. Part 1: Recovery of vertical motions and their uncertainty from airborne Doppler radial Velocity Measurements, in press at the Journal of Applied Meteorology and Climatology, https://doi.org/10.1175/JAMC-D-21-0228.1, 2022

Zelasko, N., Wettlaufer, A., Borkhuu, B., Burkhart, M., Campbell, L. S., Steenburgh, W. J., and Snider, J.R., Hotplate precipitation gauge calibrations and field measurements, Atmos. Meas. Tech., 11, 441-458, https://doi.org/10.5194/amt-11-441-2018, 2018

Zikmunda, J. and Vali, G., Fall patterns and fall velocities of rimed ice crystals, J. Atmos. Sci., 29, 1334–1347, https://doi.org/10.1175/1520-0469(1972)029<1334:FPAFVO>2.0.CO;2, 1972

Table 3 – Attenuating component concentration, one-way pathlength, and summed two-way attenuation

Date	Conc. Vapor, kg m^{-3}	Conc. Cloud Water, kg m^{-3}	Conc. Snow Particles, kg m^{-3}	Pathlength Vapor, km	Pathlength Cloud Water, km	Pathlength Snow Particles, km	Overall Two-way Attenuation, dB
15 December 2016	2.7×10^{-3}	0.01×10^{-3}	0.10×10^{-3}	1.54	1.09	1.54	0.82 [a]
3 January 2017	1.8×10^{-3}	0.08×10^{-3}	0.05×10^{-3}	1.19	0.59	1.19	0.82 [b]

[a] One-way attenuation coefficients are 0.14 dB/km for vapor (Ulaby et al. 1981), 0.052 dB/km for cloud water (Liebe et al. 1989; Vali and Haimov 2001), and 0.085 dB/km for snow particles (Nemarich et. al 1988).

[b] One-way attenuation coefficients are 0.073 dB/km for vapor (Ulaby et al. 1981), 0.45 dB/km for cloud water (Liebe et al. 1989; Vali and Haimov 2001), and 0.045 dB/km for snow particles (Nemarich et. al 1988).

1